MATERIALS SCIENCE

Lanthanide transport in angstrom-scale MoS$_2$-based two-dimensional channels

Mingzhan Wang[1]†, Qinsi Xiong[2]†, Maoyu Wang[3], Nicholas H. C. Lewis[4], Dongchen Ying[1], Gangbin Yan[1], Eli Hoenig[1]‡, Yu Han[1], One-Sun Lee[2], Guiming Peng[1]§, Hua Zhou[3], George C. Schatz[2]*, Chong Liu[1]*

Rare earth elements (REEs), critical to modern industry, are difficult to separate and purify, given their similar physicochemical properties originating from the lanthanide contraction. Here, we systematically study the transport of lanthanide ions (Ln^{3+}) in artificially confined angstrom-scale two-dimensional channels using MoS$_2$-based building blocks in an aqueous environment. The results show that the uptake and permeability of Ln^{3+} assume a well-defined volcano shape peaked at Sm^{3+}. This transport behavior is rooted from the tradeoff between the barrier for dehydration and the strength of interactions of lanthanide ions in the confinement channels, reminiscent of the Sabatier principle. Molecular dynamics simulations reveal that Sm^{3+}, with moderate hydration free energy and intermediate affinity for channel interaction, exhibit the smallest dehydration degree, consequently resulting in the highest permeability. Our work not only highlights the distinct mass transport properties under extreme confinement but also demonstrates the potential of dialing confinement dimension and chemistry for greener REEs separation.

INTRODUCTION

Rare earth elements (REEs), composed of 15 lanthanide elements (from La to Lu) and yttrium (Y) and scandium (Sc), are a unique presence in the periodic table of elements (Fig. 1A). With the progressive increase in their atomic numbers and the filling of electrons in the 4*f* orbitals, the lanthanides express themselves with two distinct characteristics. On the one hand, the unique electronic configuration of each lanthanide element endows individual elements with unique properties. These properties warrant the critical roles that REEs play in modern industry, ranging from high-performance alloys, catalysts, permanent magnets, lasers, etc. to the emerging quantum communications network[1, 2]. On the other hand, the progressive increase in atomic number leads to the monotonic shrinking of their atomic and ionic radii, i.e., the well-known "lanthanide contraction" [3, 4]. This monotonic change of atomic or ionic radii typically results in monotonic and subtle change in their physicochemical properties, e.g., Lewis acidity, hydration enthalpy, and molecular binding [1]. This monotonic and subtle change of their properties, in turn, leads to the challenges of REE separations [1, 5].

The dominant mass production of REEs includes the beneficiation of ores or other sources using concentrated acid and the subsequent separation and purification of REE both from other species and within the REE series [6]. Nonetheless, the separation and purification within the REE series are fundamentally challenging, given their similarities in physicochemical properties. Current separation methods of REEs, i.e., solvent extraction, are based on the difference in partitioning of the lanthanide ions in an organic extractant phase (e.g., TBP and HDEHP) relative to an aqueous phase (usually in a strong acidic environment) [1, 7]. The heavy use of organic extractants and acid leads to both heavy energy and environmental burdens [7, 8]. Considerable efforts have been dedicated to exploring REE separations with both higher performances and lower negative environmental impact [6, 7, 9–13]. Leading efforts have been devoted to higher-performing chelating agents, including both traditional organic extractants and recently emerging lanthanide binding peptides or proteins [14–20]. Given the global increasing needs of REE for decarbonization [21, 22], it is more urgent than ever to develop greener REE production, especially the separation and purification within the REE series [7, 8].

The extractant designing strategy for REE separation is fundamentally rooted in the different chelating strengths between the lanthanide ions and the chemical extractants, including traditional organic ones or peptide-based ones. On the other hand, nature provides unmatched examples inspiring us to separate ions. Ion (e.g., K$^+$, Na$^+$, and Ca^{2+}) channels in cell membranes, with angstrom-scale (Å-scale) physically confined space, have both high selectivity and fast conduction of corresponding ions across the cell membranes and thus play essential biological roles [23, 24]. If we can create such highly selective artificial channels for lanthanide ion separation in a mild aqueous environment, then it would revolutionize the REE purification and substantially alleviate environmental burdens and energy consumption. Along this line, it is crucially important to understand how lanthanide ions behave under the confined space associated with Å-scale channels.

Here, we systematically study the transport and separation of lanthanide ions in model Å-scale two-dimensional (2D) channels constructed with acetic acid functionalized MoS$_2$ nanosheets (MoS$_2$-COOH). We chose the trivalent REE cations (Ln^{3+}), which are the most common forms of REE cations in solution, as the model system to study. Our hypothesis underpinning the proposal is that

[1]Pritzker School of Molecular Engineering, University of Chicago, Chicago, IL 60637, USA. [2]Department of Chemistry, Northwestern University, Evanston, IL 60208, USA. [3]X-Ray Science Division, Advanced Photon Source, Argonne National Laboratory, Lemont, IL 60439, USA. [4]Department of Chemistry, Institute for Biophysical Dynamics, and James Franck Institute, University of Chicago, Chicago, IL 60637, USA.
*Corresponding author. Email: g-schatz@northwestern.edu (G.C.S.); chongliu@uchicago.edu (C.L.)
†These authors contributed equally to this work.
‡Present Address: Department of Physics and Astronomy and National Graphene Institute, The University of Manchester, Manchester, M13 9PL, UK.
§Present Address: College of Chemistry and Chemical Engineering, Jiangxi Normal University, Nanchang, Jiangxi 330022, China.
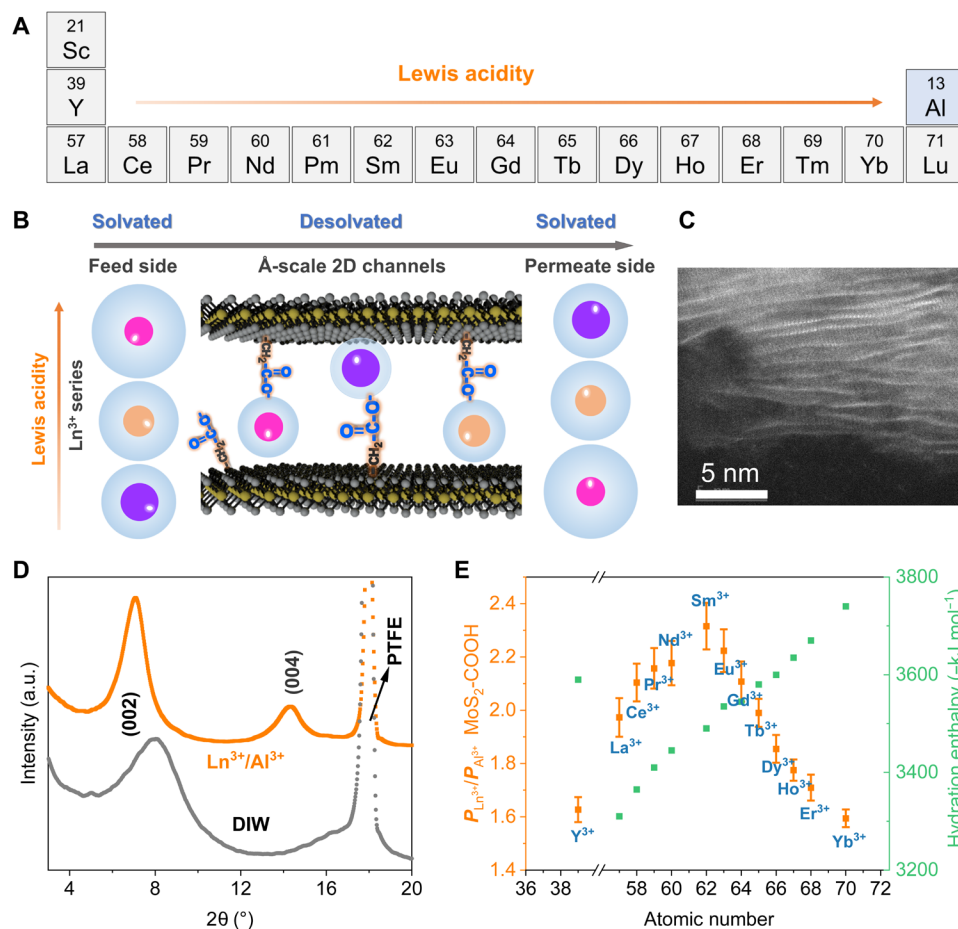
Fig. 1. Competitive transport of lanthanide ions. (**A**) The lanthanide ion series with referenced Al. (**B**) Schematic showing the transport of REE ions in the MoS$_2$-COOH 2D channels during the competitive permeation test. The anion is nitrate and omitted for clarity. (**C**) Cross-sectional STEM image of MoS$_2$-COOH membrane showing the 2D channels in the dry state. (**D**) XRD spectra of the MoS$_2$-COOH membrane in the wet state in deionized water (DIW) and Ln^{3+}/Al^{3+} mixture solution. PTFE is the substrate used. a.u., arbitrary units. (**E**) Transport results as a function of Ln^{3+} atomic number across the MoS$_2$-COOH channel.

Ln^{3+} cations with hydrated diameters ~9 Å should undergo a considerable dehydration process when passing through Å-scale confinement, whereby the corresponding dehydration energy penalty can be used to distinguish the REE cations, as previous works have shown for other ions (*25*–*30*). We observed that the permeability of lanthanide ions shows a volcano trend peaking at Sm^{3+} in such confinement in competition, deviating from the monotonic trend of single REE ion binding strength in the MoS$_2$-COOH channel without competition. X-ray absorption spectroscopy (XAS), uptake kinetics tests, and molecular dynamics (MD) simulations reveal that Sm^{3+}, being less dehydrated, enters the 2D channel much faster than the other REE ions which governs its dominating uptake. Moreover, with a slightly higher coordination number, Sm^{3+} interacts moderately with the channel which governs its fast diffusion in the 2D channel. The transport selectivity reflects a tradeoff between dehydration and binding that controls peak position in the competition of many REEs. Our work unveils the critical role of dehydration in determining the ion entrance energy (entrance sequence) and the transport energy landscape in confinement and points to the great potential for designing confinement dimension and chemistry for REE separation via transport.

RESULTS

Lanthanide transport in 2D MoS$_2$-COOH channels

For the model system, the Å-scale confinement is built by restacking MoS$_2$-COOH nanosheets [fig. S1, details of the functionalization method and membrane fabrication in Materials and Methods below and (*31*)]. The functionalization degree is ~25% per MoS$_2$. Cross-sectional scanning transmission electron microscopy (STEM) and scanning electron microscopy images show the typical layered structure of the restacked MoS$_2$-COOH membrane in its dry state (Fig. 1C and fig. S1).

We designed a concentration gradient (i.e., osmotic pressure)–driven permeation process to compare the permeation rates of Ln^{3+} across Å-scale confinement. As shown in Fig. 1B and fig. S2, a mixture containing 13 REE cations (Y^{3+}/La^{3+}/Ce^{3+}/Pr^{3+}/Nd^{3+}/Sm^{3+}/ Eu^{3+}/Gd^{3+}/ Tb^{3+}/Dy^{3+}/Ho^{3+}/Er^{3+}/Yb^{3+}) and trivalent Al^{3+} is used as the feed (~5 mM each cation, nitrate anion, pH ~3.6), and deionized water (DIW) (pH ~4 to 5) of the same volume is used as the permeate. A membrane constructed with MoS$_2$-COOH 2D Å-scale channels is mounted in between. The permeation rates of each cation from the feed to the permeate are measured. All the metal cations have the same initial molarity in the feed (~5 mM) and are always

exposed to the same environment, both external and internal, e.g., temperature, pressure, channel condition, and osmotic pressure. The interlayer spacing, which represents the channel height, was characterized by x-ray diffraction (XRD). The XRD spectra (Fig. 1D) indicate that the interlayer spacing of the MoS_2-COOH membrane in the wet state (pure DIW) is ~11.1 Å, and it increases to ~12.5 Å in the Ln^{3+}/Al^{3+} mixture solution during transport. Considering the intrinsic thickness of a monolayer MoS_2 sheet (~6.2 Å), the effective channel height for transport of the mixed ions in the MoS_2-COOH membrane is ~6.3 Å (versus ~4.9 Å in the pure DIW), implying a bilayer-water structure in the 2D channel. Moreover, XRD measurements show that the MoS_2-COOH membrane is stable in the mixture solution for a relatively long term (fig. S3).

Inductively coupled plasma mass spectrometry (ICP-MS) was used to identify and quantify individual cations in both the feed and the permeate. The concentration changes of all cations over time were simultaneously monitored (fig. S4). Water level difference was also observed, indicating water flow from the permeate to the feed (fig. S5). These observations indicate the tendency toward equilibrium across the MoS_2-COOH membrane, as confirmed by the decrease of osmotic pressure across the membrane (fig. S6). However, the ions show three different concentration profiles in the test window: equilibrium, nonequilibrium, and crossover between the feed and the permeate (fig. S4). The qualitative difference suggests that the ions have different transport speeds across the MoS_2-COOH 2D channels.

Quantitative analyses are further made based on the permeation rates, P_i (mol/s) (see calculation details in Material and Methods). Al^{3+} is used as the reference. The relative ion permeation rates of lanthanide ions versus Al^{3+}, $P_{Ln^{3+}}/P_{Al^{3+}}$, across the MoS_2-COOH channels range from ~1.6 to ~2.3. This fact indicates that Ln^{3+} can permeate through the 2D channel much faster than Al^{3+}. This can be attributed to the fact that Al^{3+} has the largest hydration enthalpy in the group: the hydration enthalpy of Al^{3+} is −4715 kJ/mol, much larger than that of Yb^{3+}, −3740 kJ/mol (32). Since the hydration enthalpy characterizes the interactions between ions and water molecules within their hydration shells, larger ionic hydration enthalpy also indicates larger ionic hydration radius in bulk solution and larger energy barrier for ions to overcome when passing through the confinement. $P_{Ln^{3+}}/P_{Al^{3+}}$ values show a clear volcano shape peaking at Sm^{3+} (Fig. 1E and fig. S7). This observation is uncommon for the lanthanides, given that lanthanides typically show monotonic property changes due to the lanthanide contraction mentioned above. We note that this volcano-shaped transport behavior is robust in all tests using different MoS_2-COOH membranes (fig. S7B). Similar volcano shape is also observed when Na^+ is used as the reference, although $P_{Ln^{3+}}$ are ~3- to 5-fold smaller than P_{Na^+} (fig. S8). Likewise, this can be attributed to the much smaller hydration enthalpy of Na^+ (−405 kJ/mol). In addition, changing the lanthanide ion combination (using $Y^{3+}/La^{3+}/Ce^{3+}/Nd^{3+}/Eu^{3+}/Tb^{3+}/Dy^{3+}/Yb^{3+}$) results in a similar volcano shape in transport (fig. S9). As a comparison, a commercial porous polytetrafluoroethylene (PTFE) membrane (nominal pore size, ~200 nm) was used for the transport test. Experimental measurement shows that $P_{Ln^{3+}}/P_{Al^{3+}}$ decreases monotonically with increase in atomic number when passing through the PTFE membrane (fig. S10). The monotonic decrease for the PTFE membrane is consistent with the change of bulk diffusion coefficients (33, 34) and can be explained by the monotonic increase in hydration enthalpy. Notably, although the adjacent pair selectivity in the MoS_2-COOH 2D channels is lower than those in organic extractants, ranging from ~1.01 to ~1.07, it is higher than those in the PTFE membrane (or the bulk) with typical values below 1.01 (fig. S11). This comparison suggests that confinement can be a tool used to enhance the separation selectivity of REE ions. To explain the uncommon volcano shape in the transport trend observed for lanthanide ions in the 2D channels, we examined the thermodynamics and kinetics of REE cations in the MoS_2-COOH channels.

Thermodynamics

First, the ion uptake in the mixture solution was measured. The results indicate that the uptake amounts of REE cations in the MoS_2-COOH membrane also show a clear volcano shape, peaking at Sm^{3+} (figs. S12 and S13). Independent uptake tests using the MoS_2-COOH membrane show that the binary separation values between La^{3+}/Ce^{3+}, La^{3+}/Yb^{3+}, Sm^{3+}/La^{3+}, and Sm^{3+}/Yb^{3+} are ~1.4, ~1.4, ~2.5, and ~1.7, respectively (fig. S14). Given that the coordination modes between Ln^{3+} and lanthanide binding proteins (e.g., lanmodulin) play an important role (17, 19, 20), we probed the ion coordination in 2D MoS_2-COOH using infrared (IR) spectroscopy. On the basis of the ion-carboxylate coordination peak position, Ln^{3+} adopt a combination of monodentate and bidentate binding modes with the carboxylate groups, while Al^{3+} only adopts the monodentate binding mode (Fig. 2, A and B) (35). The single ion uptake results show that the uptake amounts follow an increasing trend with heavier REE ions having larger uptake, which indicates stronger interactions between heavier REE and the MoS_2-COOH (fig. S15). The stronger interactions between the heavier REE ions with the MoS_2-COOH walls can be further corroborated by the XRD measurements of single salt treated MoS_2-COOH membranes. With increase in the atomic number of Ln^{3+}, the right shift of both (002) and (004) peaks suggests a decrease in the interlayer spacing in the MoS_2-COOH channel (Fig. 2, C to E). Note that the hydration radius in the bulk solution is expected to increase with atomic number, given the increase in their Lewis acidity (36). In other words, the decreasing trend of the interlayer spacing in the single Ln^{3+} treated MoS_2-COOH channel is exactly against their ionic hydration radius trend, which thus should be attributed to stronger interactions between heavier REE ion and the MoS_2-COOH walls.

Then, we turned to synchrotron XAS to probe the coordination environment of REE ions in the 2D confinement (Fig. 2F and fig. S16, details in Materials and Methods below). The fitting results are listed in table S1. The result shows that in bulk solution, light REE ions (La^{3+}/Sm^{3+}) have ~9 water molecules, and the heavy REE ion (Dy^{3+}) has ~8 water molecules in their first hydration shell, consistent with both previous experimental results (37) and MD simulations (34). By comparison, in 2D confinement, the coordination number of Sm^{3+} decreased by ~3.0, and La^{3+} and Dy^{3+} decreased by 3.3. This result has two implications. First, a significant amount of dehydration in the first hydration shell occurred for REE ions adsorbed in the 2D MoS_2-COOH channels, indicating a critical role of the dehydration barrier for transport in confinement; second, the dehydration degree is different among REE ions with Sm^{3+} having less dehydration. The larger degree of dehydration for La^{3+} could be due to its larger bare ion size such that it requires a smaller coordination number to fit into the channel. The larger degree of dehydration for Dy^{3+} could be resulting from the stronger interaction with the MoS_2-COOH channel. On the basis of the results, we propose an intuitive picture, purely from the perspective of thermodynamics, to
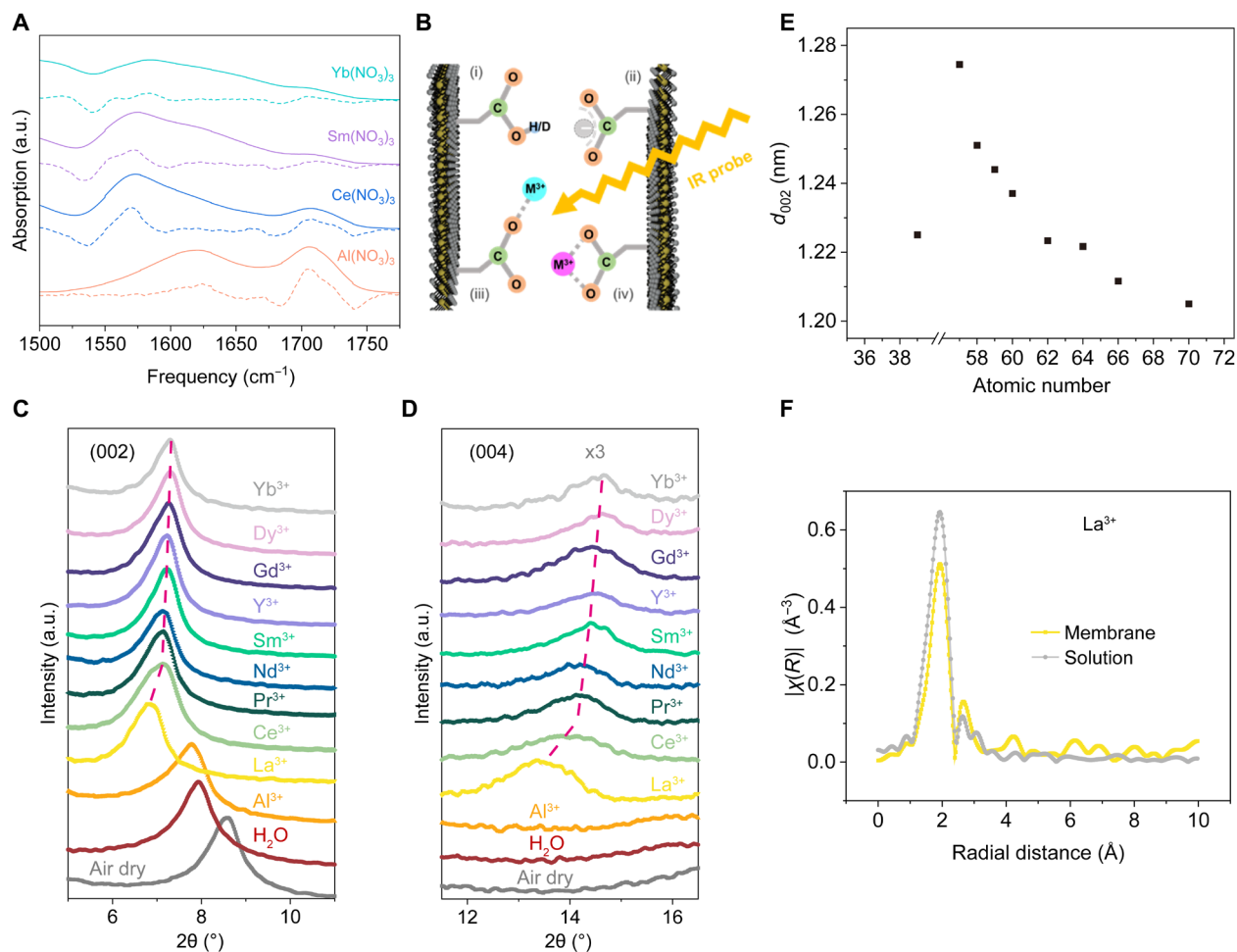
Fig. 2. Structures of lanthanide ions in the 2D channels. (**A**) The effect of different metal cations on the IR absorption spectra of the carboxylate group in the MoS_2-COOH membranes. The dashed lines are the corresponding negative second-order derivatives of the absorption spectra (solid lines) for peak pinpointing. (**B**) Schematic illustrations of the protonated/deuterated carboxylate group (i), free carboxylate group (ii), the monodentate (iii), and bidentate (iv) coordination mode between metal cations and carboxylate group. (**C** and **D**) The (002) and (004) peaks of the XRD spectra of the MoS_2-COOH membrane with individual Ln^{3+}/Al^{3+} ions, respectively. Note that (004) peak is absent in the air-dry sample, DIW-soaked sample and the Al^{3+}-soaked sample. Except for the air-dry sample without any ions, other samples were measured in their wet state. (**E**) The interlayer spacing change of the MoS_2-COOH channel with individual Ln^{3+} ions in the wet state. (**F**) EXAFS spectra of La^{3+} in the bulk solution and in the MoS_2-COOH membrane.

explain the volcano shape of the uptake result observed in the 2D confined channels. With the increase in the atomic number, the increase of Lewis acidity (or the shrinking of ionic radii) of REE ions plays a dual role: On one hand, heavier REE ions would have stronger interactions with the MoS_2-COOH walls, which thus translate into their thermodynamic advantages in confinement; on the other hand, heavier REE ions would have a higher dehydration energy penalty to overcome when going from the bulk solution into the 2D channels. Therefore, the tradeoff between the dehydration barrier and strength of interactions for the Ln^{3+} ions in 2D confinement leads to the volcano shape observed, a mechanism reminiscent of the Sabatier principle well-established in catalysis (*38*) and reported recently for designing ultrastable nanocatalysts (*39*).

We noticed that for the MoS_2-COOH membrane uptake results, the single ion uptake pattern (increasing trend) is notably different from that for the REE mixture (volcano trend). This difference can be explained from the changes in thermodynamics and the membrane uptake kinetics. Take Yb^{3+} as an example. In the single-solute solution, Yb^{3+} exhibits the smallest interlayer spacing (~12.0 Å) in its thermodynamically stable state among REE ions. By comparison, in the mixture uptake experiment, the interlayer spacing is ~12.5 Å (Ln^{3+}/Al^{3+} mixture; Fig. 1D) or 12.9 Å (Ln^{3+} mixture without Al^{3+}; see "pH effect"), larger than the thermodynamically stable interlayer spacing for the single Yb^{3+}. Thermodynamically, the larger interlayer spacing leads to a reduction in the binding affinity between Yb^{3+} ions and MoS_2-COOH, which is consistent with the decrease in uptake found in the mixed ion experiment. In addition, as will be comprehensively discussed in the next section ("MD simulations and kinetics"), the kinetics of ion entrance to the channels and ion interaction in the channels also play significant roles, and this is important to both uptake and transport.

MD simulations and kinetics

To further advance our understanding of ion transport within 2D MoS_2-COOH channels, we conducted all-atom MD simulations (Fig. 3A). The interlayer spacing (Mo-Mo distance) was set to be 12.5 Å, consistent with the experiment (more details in the Supplementary Materials). We simulated ion transport from the feed into the channel by applying high pressure to the piston wall (Fig. 3A). The fluxes of REE cations into the channel and into the permeate are depicted in Fig. 3B. Notably, the flux of cations into the permeate effectively reproduces the experimentally observed volcano shape of the REE cations across the MoS_2-COOH channel (Fig. 1D). The greater initial flux of cations into the channel compared to that into the permeate can be attributed to the high-energy barrier arising

from the attractive electrostatic interactions between REE cations and —COOH/—COO⁻ groups inside the MoS_2-COOH channel. In addition, these findings indicate that Sm^{3+} exhibits the fastest uptake from the feed into the channel. The dynamics of membrane uptake using the REE mixture solution was tested in our measurements, and indeed the uptake of Sm^{3+} shows the fastest uptake rate into the membrane (Fig. 3C), which is consistent with the MD simulations. Please note that the simulated mixture used in this study represents a simplified model in comparison to the experimental setup (details in the Supplementary Materials). Nonetheless, the trends extracted from our simulations align coherently with the experimental observations and provide atomistic-level insight into the underlying mechanisms governing ion transport.
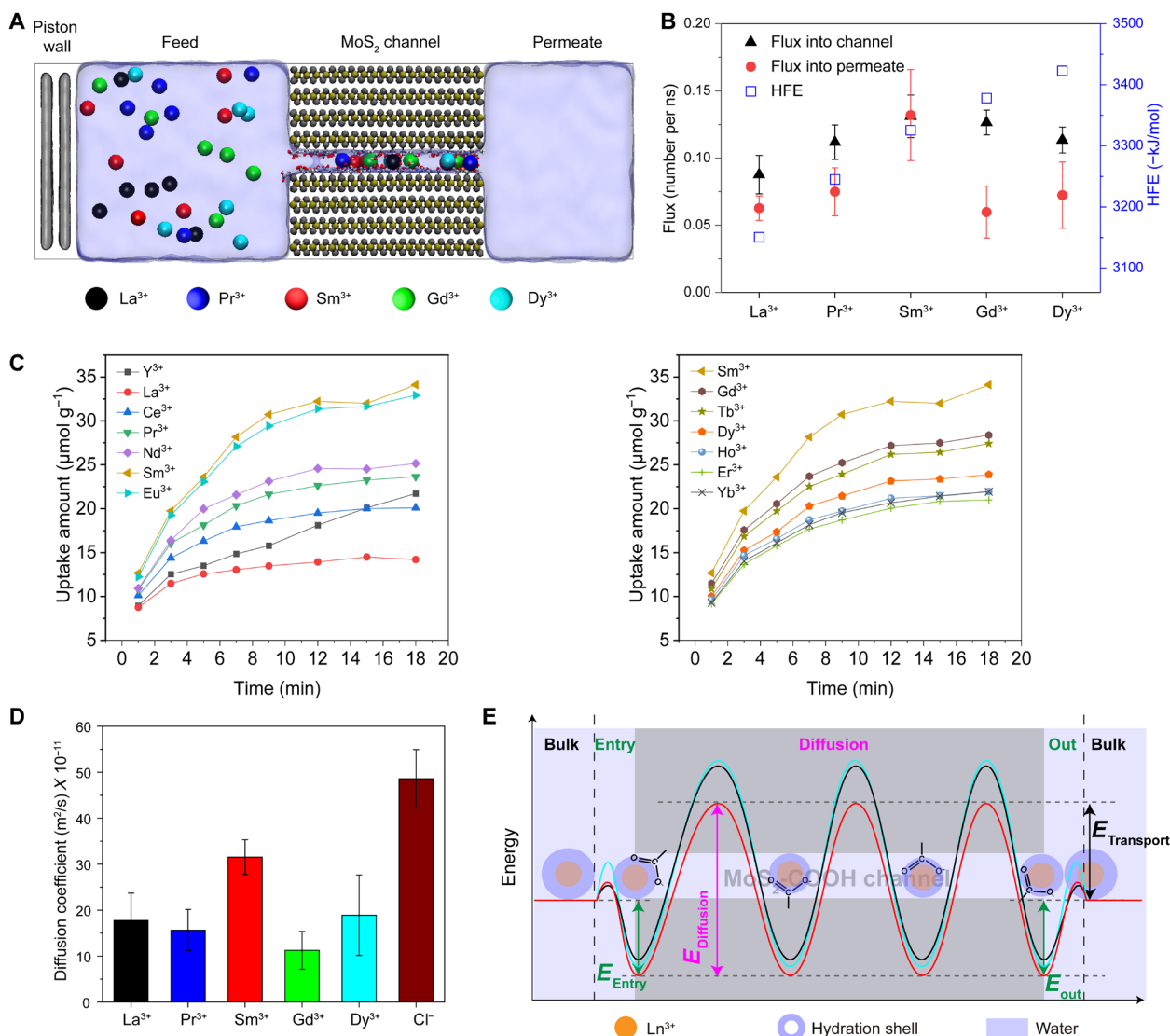

Fig. 3. MD simulations and kinetics. (**A**) Simulation modeling of REE cations transport through 2D MoS_2-COOH channels, which includes six extra MoS_2 sheets as the supporting membrane (Mo in yellow and S in gray), water (transparent blue), ions (in black, blue, red, green and cyan) and two MoS_2 sheets as piston wall (in gray). (**B**) MD simulations results showing the fluxes of REE cations into the MoS_2-COOH channel, the fluxes of REE cation into the permeate, and the hydration free energy (HFE). Here, the flux in this study is determined by linearly fitting the time evolution of ion entry into the channel or into the permeate. Our analysis is confined to the times where the ion counts increase most rapidly. (**C**) Experimental data showing the dynamics of Ln^{3+} uptake in the MoS_2-COOH membrane. Note that Sm^{3+} is plotted in both figures for better comparison. (**D**) Averaged diffusion coefficients of Ln^{3+} cations and Cl^- anions in the MD simulations. (**E**) A schematic diagram of the energy barrier landscape for REE cations transport in the MoS_2-COOH channel. The color of the curves is chosen to match that of the bars for the same element in (D).

Subsequently, we performed calculations to determine the diffusion coefficients of REE cations and Cl$^-$ anion (see Fig. 3D and fig. S19). The diffusion coefficients of REE cations entering and passing through the channel both showed a volcano-shaped pattern, with Sm^{3+} exhibiting the highest diffusion coefficient. The diffusion coefficient of Cl$^-$ is 1.5 to 4 times higher than that of REE cations, suggesting that Cl$^-$ does not significantly participate in the diffusion of REE cations. To further confirm this, we evaluated the ratio of REE cations that pass through the membrane and the ratio of REE cations that are knocked (i.e., interact at a distance that is 3.5 Å or less) by Cl$^-$ and pass through the membrane, respectively (fig. S20). Our analysis revealed a lack of correlation between these two ratios, indicative of the independent transport of REE cations and Cl$^-$ anions as they permeate the MoS$_2$-COOH channel. This indicates that ion-pair formation is not significant to the transport.

Factors such as ion pairing, dehydration, and the interaction between ions and membranes are recognized as primary determinants governing the ion transport mechanism (40). Given that ion pairing is not important to the observed volcano shape, our subsequent focus shifts to elucidating the dehydration effect and ion-membrane interactions. We first computed the hydration free energy (HFE) of REE cations in the bulk solution (see Fig. 3B), which reveals a positive correlation with the atomic number, aligning with the tabulated hydration enthalpy values in Fig. 1E. Furthermore, we performed a series of umbrella sampling simulations to obtain the potential of mean force (PMF) for REE cations permeating the membrane (fig. S21). According to the PMF results, we categorized the difficulty of ion permeation into three levels: "easy penetrating," including La^{3+} and Pr^{3+} cations (level I); "medium penetrating," represented by Sm^{3+} (level II); and "difficult penetrating," including Gd^{3+} and Dy^{3+} (level III). It is important to note that the PMF displays variability when distinct pathways are selected, as depicted in fig. S22, and our PMF simulations focus on the transport of individual ions rather than a mixture of ions. Therefore, the PMF data provided serve exclusively as a reference for evaluating the binding affinity between REE cations and —COOH/—COO$^-$ groups and should not be construed as an accurate representation of actual permeation phenomena for REE mixtures.

The results above indicate that Sm^{3+} exhibits a moderate degree of HFE and binding affinity with —COOH/—COO$^-$ groups, consistent with the experimental measurements (Fig. 2, C to F). To gain insight into its impact on the dehydration effect during permeation, we investigated changes in the coordination number within the first solvation shell of the REE cations (fig. S23). On the one hand, the La^{3+} and Pr^{3+} cations can more easily lose or gain water (1 to 2 water) during the process of passing through the channel, attributable to their weaker HFE and binding affinity with —COOH/—COO$^-$ group. On the other hand, because of their robust binding affinity with the —COOH/—COO$^-$ group, Gd^{3+} and Dy^{3+} cations experienced a loss of 0.8 to 1.1 water molecules during the permeation process. Together with their higher HFE, these ions encountered the highest-energy barrier while traversing the channel. Unexpectedly, the Sm^{3+} cation, which has an intermediate HFE and binding affinity with the —COOH/—COO$^-$ group, exhibited the lowest degree of dehydration (0.2 to 0.5 water) when passing through the channel, which is in qualitative agreement with XAS data (table S1) and thus results in the highest permeation rate. Note that the dehydration number we extract here is the dehydration number for transport, which is different from the dehydration number for uptake that was extracted from the XAS data. In addition, we

examined the dwell time of REE cations in the vicinity (3.5 Å) of —COOH/—COO$^-$ groups, which reveals a positive correlation with atomic number, with the exception of the Sm^{3+} cation (fig. S24). This observation is consistent with the fact that the Sm^{3+} cation experiences the least dehydration during permeation.

On the basis of the above discussion and previous studies (40–42), we propose a diagram to qualitatively illustrate the energy barrier landscape for REE cation transport in MoS$_2$-COOH channels (Fig. 3E). In the entry phase, REE cations undergo a dehydration penalty and electrostatic attraction reward with the MoS$_2$-COOH channel. These factors collectively contribute to a kinetically determined dehydration barrier at the entrance to the channel and then a well once the ions coordinate to acetate near the entrance. If we denote the difference between the barrier and well energies as E_{Entry}, then the effective diffusion coefficient of cations entering the channel is determined by ($E_{Entry} \sim RTlnD_{Entry}$) (3). As depicted in (Fig. 3 B to D), the Sm^{3+} cation exhibits the fastest uptake (largest D_{Entry}) from the solution into the membrane for mixed ion transport, implying that this cation should have the largest value of E_{Entry}. Likewise, the energy barrier governing intramembrane diffusion ($E_{Diffusion}$) can be inferred from the diffusion coefficient within the membrane ($E_{Diffusion} \sim -RTlnD_{Diffusion}$) (fig. S19), suggesting that Sm^{3+} cation has the lowest $E_{Diffusion}$ (Fig. 3E for mixed transport). Consequently, Sm^{3+} holds the lowest-energy barrier for ion transport through the membrane ($E_{Transport}$), thereby manifesting the highest permeability. Further, MD simulations show that a slight increase (5%) in the channel height leads to REE transport behavior deviating from the volcano shape, indicating its sensitivity to the confinement dimension (fig. S25).

pH effect

Further data analysis reveals a prominent fact in the uptake: The ratios of Ln^{3+} to —COOH ($\sum N_M^{3+}/N_{-COOH}$) in all the membrane uptake tests using mixed REE solution with concentration ranging from 0.1 to 10 mM (corresponding pH range from ~3.6 to ~4.7; fig. S12) are only around 30%. This fact further leads us to a question: What is the role of the protonation/deprotonation of —COOH in the uptake and transport? To approach this question, we conducted membrane uptake experiments at different pH values, ranging from ~4.7 to ~7.1 (concentration: 0.1 mM, details in Materials and Methods below). The result is shown in Fig. 4A. At pH ~4.7, the membrane uptake of Ln^{3+} basically shows a volcano shape peaking at Sm^{3+}, consistent with the aforementioned results. However, upon increase in pH, the uptake amount of Ln^{3+} increases due to enhanced deprotonation. Further analyses show that the ratio of $\sum N_M^{3+}/N_{-COOH}$ is likely to increase to over 100% at pH ~7.1 (table. S2), which points to the possibility of Ln^{3+} coordinating with sulfur atoms in the MoS$_2$-COOH 2D channels. Meanwhile, the shape of the Ln^{3+} uptake curve gradually changes into a monotonically increasing function as pH increases. This presumably reflects a change in the tradeoff between dehydration penalty and electrostatic attraction when the —COOH gets deprotonated as pH is increased. It is also noteworthy that there seems to be a discontinuity in the curves in Fig. 4A at Gd^{3+} (atomic number 64). This might suggest the empirical "Gadolinium break" argument for REEs (43), which remains to be clarified.

XRD measurements show that the interlayer spacing of the MoS$_2$-COOH 2D channels increases from 12.9 Å at pH ~4.7 to 13.5 Å at at pH ~7.1 (Fig. 4B). This suggests that the enlarged channel
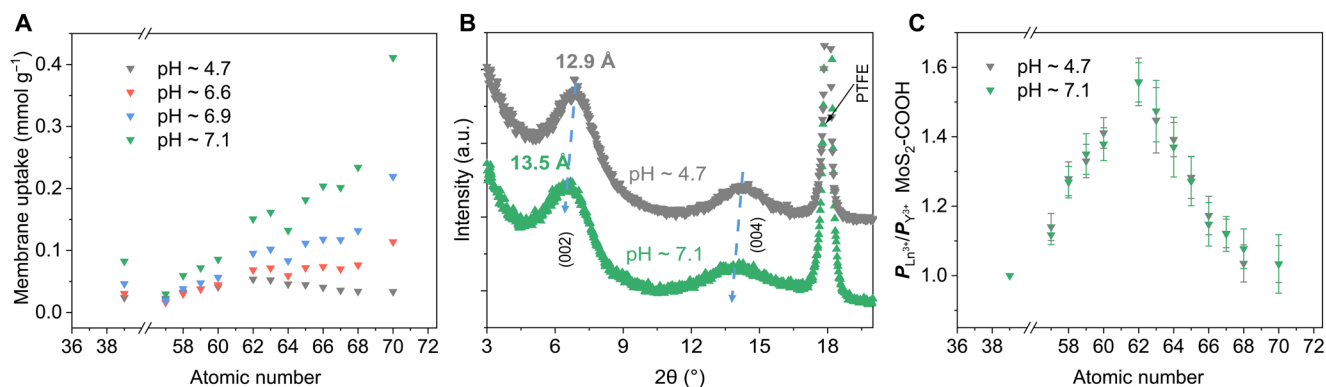
Fig. 4. pH effect on uptake and transport. The uptake (**A**), interlayer spacing (**B**), and permeation rate (**C**) of Ln^{3+} in the MoS_2-COOH channels at different pH values.

spacing will decrease the dehydration penalty for Ln^{3+} entering into the 2D confinement. Therefore, at high pH, the enhanced binding due to enhanced deprotonation and the decreased dehydration barrier due to enlarged interlayer spacing break the tradeoff between dehydration and strength of interactions with confinement channels, which in turn contributes to the enhanced uptake of heavier Ln^{3+} (Fig. 4A). However, in the transport experiments (details in Materials and Methods below), the permeability of Ln^{3+} at both pH ~7.1 and pH ~4.7 shows a similar volcano shape (Fig. 4C and fig. S26), which is unexpected given that the uptake trend is different at different pHs. A possible scenario we propose here is that a significant fraction of Ln^{3+} ions that are absorbed into the 2D channels, particularly the heavier ones, is trapped. Thus, their thermodynamic advantage (larger uptake) does not straightforwardly translate into a higher permeabilty in the 2D channel. More efforts are needed to clarify the difference between uptake and transport at high pH nonetheless.

Given that the tradeoff of Ln^{3+} cannot be fine-tuned by pH in the MoS_2-COOH channels, we tried to explore Ln^{3+} transport in the 2D confinement by changing the confinement environment as a final effort. In the pristine MoS_2 channels without any functionalization or with amide-functionalized MoS_2 (MoS_2-$CONH_2$) channels (*31*), what we observed is basically a monotonically decreasing trend, instead of a volcano shape, for P_{Ln}^{3+} as a function of atomic number (figs. S27 and S28), suggesting a lack of the tradeoff noted above. All combined, we conclude that the tradeoff enabling the volcano shape observed is sensitive to both the confinement dimension and confinement chemistry.

DISCUSSION
To sum up, we systematically studied the transport of lanthanide ions in model Å-scale 2D MoS_2-COOH channels in an aqueous environment. A volcano-shaped transport trend of lanthanide ions is observed. Both the thermodynamics and kinetics of ion transport under 2D confinement are systematically analyzed. The results indicate that controlling the dehydration degree and binding strength of lanthanide ions in the 2D channel are critical in governing a smooth energy landscape for transport. Our current experimental and MD simulations results point to the possibility of tuning REE selectivity with different functional groups in the 2D channels. It also implies the possibility of achieving REE separations in 1D or 0D confinement

with delicate functionalization. All these efforts would facilitate the inverse design of selective REE separation materials.

MATERIALS AND METHODS
Preparation of mixed ions solution
$Al(NO_3)_3 \cdot 9H_2O / La(NO_3)_3 \cdot 6H_2O / Ce(NO_3)_3 \cdot 6H_2O / Pr(NO_3)_3 \cdot 6H_2O / Nd(NO_3)_3 \cdot 6H_2O / Sm(NO_3)_3 \cdot 6H_2O / Eu(NO_3)_3 \cdot 6H_2O / Gd(NO_3)_3 \cdot 6H_2O / Tb(NO_3)_3 \cdot 6H_2O / Dy(NO_3)_3 \cdot 5H_2O / Ho(NO_3)_3 \cdot 5H_2O / Er(NO_3)_3 \cdot 5H_2O / Yb(NO_3)_3 \cdot 5H_2O$ were used as salts. $Al(NO_3)_3 \cdot 9H_2O$ (98 + %) was purchased from Strem Chemicals. All REE salts were purchased from Neta Scientific Inc. with 99 + %purity. All chemicals were used without further treatment.

The concentration of aqueous Al^{3+}/Ln^{3+} mixture solution was ~5 mM for each cation with intrinsic pH ~3.6. Note that all the salt solutions used in the tests, either the single salt solution or the mixture solutions of varied combinations, have intrinsic pH values (typically acid) after salt dissolve without further tuning, unless stated below.

To explore the pH effect for REE separation, we chose a low concentration of Ln^{3+} mixture solution (~0.1 mM with intrinsic pH ~4.7) to enlarge the tunability of the pH window. KOH aqueous solution (0.5 M) was used to tune the pH of Ln^{3+} mixture solution. No precipitation was observed when pH of the Ln^{3+} mixture solution was tuned up to ~7.2. Further, increasing the pH leads to the precipitation of Ln^{3+}. For the same reason, Al^{3+} was kicked out of the Ln^{3+} mixture, because it precipitated out upon the addition of KOH.

Preparation of MoS₂-COOH dispersion solution
First, the single- or few-layer MoS_2 nanosheet aqueous dispersion solution was prepared through the intercalation of MoS_2 powders (Sigma-Aldrich) in *n*-butyl lithium/hexane solution (1.6 M) (Caution!), as widely reported previously. Then, the acetic acid functionalization of the MoS_2 nanosheet was achieved through its nucleophilic reaction with iodoacetic acid (ICH_2COOH, purchased from Sigma-Aldrich), as we reported in (*31*) of the main text. Our previous measurement shows that the functionalization degree is ~25% —COOH per MoS_2.

Preparation of MoS₂-COOH membrane
Before membrane preparation, to remove possible ion contaminations, the prepared MoS_2-COOH dispersion solution is washed with

dilute trace-metal HCl (~2 to 5 mM), which is followed by filtration and redispersion in water under sonication (~10 to 15 min). The "HCl washing-filtration-redispersion" cycle was repeated at least three times. Then, the redispersed MoS_2-COOH solutions is dialyzed in dialysis tubings (Sigma-Aldrich, part no. D9527-100FT) to remove extra HCl. Last, repeated centrifugation (~4000 rpm/10 min) is used to get the aqueous dispersion solutions of single- or few-layer MoS_2-COOH nanosheets (concentration, 0.1 to 0.2 mg/ml), which were stored in HCl-washed plastic bottles and under 4°C for use.

The MoS_2-COOH membrane is prepared via the vacuum-assisted filtration method. The substrate used is PTFE (fig. S10,; pore size: 0.2 μm; purchased from Sigma-Aldrich, part no. JGWP04700). Upon filtration, the MoS_2-COOH/PTFE complex membrane is transferred to clean petri dishes for overnight air drying. Note that to avoid membrane shrinkage or deformation, before membrane transfer, several drops of DIW is put beneath the complex membrane to remove air bubbles between PTFE and dishes. Then, the air-dried complex membrane is used for ion transport tests, membrane uptake tests, and other characterizations like XRD and XAS tests. Our previous study (31) shows that the as-prepared MoS_2-COOH composite membrane has good mechanical strength, which can withstand high pressure at least >10 bar.

The competitive permeation test of mixed ions across the membranes
Experimental protocol
A pair of H-cells was used for the competitive permeation test of mixed ions across the membranes, including the porous PTFE membrane and MoS_2-COOH/PTFE complex membrane. These membranes are mounted in between the H-cells by commercial Silicon paste. The H-cells are ready for permeation tests upon solidification of the Silicon paste.

In a competitive permeation test of mixed ions, 21 ml of solution of mixed ions (either 5 mM Al^{3+}/Ln^{3+} mixture or Ln^{3+} mixture) and 21 ml of DIW were simultaneously poured into the feed side and the permeate side of H-cells, respectively. For the transport test using 0.1 mM Ln^{3+} with pH 7.1 (fig. S26), the pH of the DIW in the permeate side was tuned to be ~7.1 at the very beginning of the test. Note that the MoS_2-COOH faces the feed side for the MoS_2-COOH/PTFE complex membrane. Both chambers are strongly stirred to avoid concentration polarization throughout the permeation tests. Then, the concentration changes of every metal cation were monitored through periodic samplings (10 to 100 μl per sampling subject to change according to permeation time), which were then diluted by 3% HNO_3 to 3 to 5 ml for ICP-MS measurements. Both chambers were tightly sealed with parafilm to avoid undesired evaporation throughout the process, except when sampling.
Quantitative analyses
To perform quantitative analysis, we focus on the ion concentration changes in the permeate side in the early stage, which show a linear increase versus time (figs. S7A, S8, A to C, S9A, S10D, S26, S27A, and S28A). By calculating the slopes of linear profiles, we can get the permeation rates of all the ions, P_i (mol/s). The permeation rate of Al^{3+} or Y^{3+} or Na^+ is used as a reference. P_i values are plotted. We note here that although a level difference between the feed chamber and the permeate chamber can be always observed in the long-time test, this difference was very small in the early stage for a few hours and volume changes of both chambers were typically <2%.

The IR tests
The prepared MoS_2-COOH membranes were transferred from the PTFE substrate to 1-mm-thick CaF_2 substrates for IR absorption measurements. Before IR measurements, the membranes were soaked in individual salt solution (1 M in D_2O, purchased from Fisher Scientific, part no. M1133660100) overnight to achieve ion uptake equilibrium and were gently dried with tissue to remove the excess water immediately before the measurement. All spectra were measured in a Bruker Hyperion microscope coupled to a Bruker Vertex 70 FTIR spectrometer. The measurements were performed with a 0.4–numerical aperture (NA) Schwarzschild objective resulting in an IR focal spot of 100-μm diameter. Measurements were repeated to ensure the region of the sample was spatially uniform. Spectra were measured with a 2-cm^{-1} resolution, and 32 scans were averaged. The second derivative spectra were determined using a differentiating Savitztky-Golay filter.

Membrane uptake test
MoS_2-COOH membranes were soaked into relevant solutions for at least overnight to achieve uptake equilibria. Note that for the membrane uptake kinetics test in Fig. 3B, the uptake time lasted for given durations as shown. After membrane uptake test, the membrane was taken out and thoroughly washed with flowing DIW (for ~2 min) to remove the mixed ions solution remaining on the surface. Then, the washed membranes were dissolved in 3 ml of HNO_3 (3%) under sonication overnight. Last, the leaching HNO_3 solution was filtered and diluted for ICP-MS measurement.

XAS measurement
MoS_2-COOH membrane was soaked in the mixture solution of $La^{3+}/Pr^{3+}/Sm^{3+}/Gd^{3+}/Dy^{3+}/Yb^{3+}$(~5 mM, natural pH after salts dissolving without tuning). This mixture combination is to increase the loading of each single REE cation to increase the signal-to-noise ratio in XAS measurements while maintaining the volcano-shaped uptake observed (as confirmed in fig. S13B).

XAS experiments were carried out at 5BM-DND, Advanced Photon Source of Argonne National Laboratory. All the K-edge XAS measurements of La^{3+}, Sm^{3+}, and Dy^{3+} were conducted under fluorescence mode by a Vortex ME4 detector. All XAS data analyses were performed with Athena software package to extract x-ray absorption near-edge structure and extended x-ray absorption fine structure (EXAFS). Fourier transform of La^{3+}, Sm^{3+}, and Dy^{3+} was performed by using Hanning window function with k-weights of 2 and k-range from 3 to 10 Å^{-1}. For model-based EXAFS analysis, all the scattering paths were generated by the FEFF calculation function in Artemis based on the crystal structure of $La(H_2O)_9$, $Sm(H_2O)_9$, and $Dy(H_2O)_8$. The generated scattering paths were then calibrated by performing the FEFF of the EXAFS data of those reference solution samples, mainly to obtain the amplitude reduction factor (S_0^2) values. With S_0^2 known, all EXAFS data of the membranes were fitted.

All-atom MD simulations
We performed all-atom MD simulations to study the cooperative transport of mixed REE ($La^{3+}/Pr^{3+}/Sm^{3+}/Gd^{3+}/Dy^{3+}$) cations in the MoS_2-COOH membranes. Our model (Fig. 3A) consists of a bilayer MoS_2 sheet acting as a rigid piston wall to exert external pressure, an ion-filled feed region, a multilayered MoS_2 membrane serving as an ion channel, and a pure water permeate region. The multilayered MoS_2 membrane can be visualized as extracting two

layers of MoS_2 from bulk crystals (2H-MoS_2) and being modified with corresponding acetate functional groups while leaving a 12.5-Å interlayer spacing (Mo-Mo distance) that is consistent with the experiment. Other MD simulations details are provided in the Supplementary Materials.

Supplementary Materials

This PDF file includes:

Figs. S1 to S28
Table S1 to S3
Notes S1 to S3

REFERENCES AND NOTES

1. T. Cheisson, E. J. Schelter, Rare earth elements: Mendeleev's bane, modern marvels. *Science* **363**, 489–493 (2019).
2. H. Zhang, H. Zhang, Special Issue: Rare earth luminescent materials. *Light Sci. Appl.* **11**, 9 (2022).
3. K. J. Laidler, The development of the Arrhenius equation. *J. Chem. Educ.* **61**, 494 (1984).
4. S. C. Bart, What is the "Lanthanide Contraction"? *Inorg. Chem.* **62**, 3713–3714 (2023).
5. D. S. Sholl, R. P. Lively, Seven chemical separations to change the world. *Nature* **532**, 435–437 (2016).
6. B. Deng, X. Wang, D. X. Luong, R. A. Carter, Z. Wang, M. B. Tomson, J. M. Tour, Rare earth elements from waste. *Sci. Adv.* **8**, eabm3132 (2022).
7. C. Liao, S. Wu, F. Cheng, S. Wang, Y. Liu, B. Zhang, C. Yan, Clean separation technologies of rare earth resources in China. *J. Rare Earths* **31**, 331–336 (2013).
8. J. C. K. Lee, Z. Wen, Pathways for greening the supply of rare earth elements in China. *Nat. Sustain.* **1**, 598–605 (2018).
9. H. Fang, B. E. Cole, Y. Qiao, J. A. Bogart, T. Cheisson, B. C. Manor, P. J. Carroll, E. J. Schelter, Electro-kinetic separation of rare Earth elements using a redox-active ligand. *Angew. Chem. Int. Ed.* **56**, 13450–13454 (2017).
10. W. D. Bonificio, D. R. Clarke, Rare-Earth separation using bacteria. *Environ. Sci. Technol. Lett.* **3**, 180–184 (2016).
11. G. Wang, J. Xu, L. Ran, R. Zhu, B. Ling, X. Liang, S. Kang, Y. Wang, J. Wei, L. Ma, Y. Zhuang, J. Zhu, H. He, A green and efficient technology to recover rare earth from weathering crusts. *Nat. Sustain.* **6**, 12 (2023).
12. Z. Zhang, Q. Jia, W. Liao, "Progress in the Separation Processes for Rare Earth Resources" in *Handbook on the Physics and Chemistry of Rare Earths* (Elsevier, 2015; https://linkinghub.elsevier.com/retrieve/pii/B9780444634832000041) vol. 48, pp. 287–376.
13. T. Uda, K. T. Jacob, M. Hirasawa, Technique for enhanced rare Earth separation. *Science* **289**, 2326–2329 (2000).
14. A. G. Baldwin, A. S. Ivanov, N. J. Williams, R. J. Ellis, B. A. Moyer, V. S. Bryantsev, J. C. Shafer, Outer-sphere water clusters tune the lanthanide selectivity of diglycolamides. *ACS Cent. Sci.* **4**, 739–747 (2018).
15. J. A. Bogart, B. E. Cole, M. A. Boreen, C. A. Lippincott, B. C. Manor, P. J. Carroll, E. J. Schelter, Accomplishing simple, solubility-based separations of rare earth elements with complexes bearing size-sensitive molecular apertures. *Proc. Natl. Acad. Sci. U.S.A.* **113**, 14887–14892 (2016).
16. P. J. Panak, A. Geist, Complexation and extraction of trivalent actinides and lanthanides by triazinylpyridine N-donor ligands. *Chem. Rev.* **113**, 1199–1236 (2013).
17. J. A. Mattocks, J. J. Jung, C.-Y. Lin, Z. Dong, N. H. Yennawar, E. R. Featherston, C. S. Kang-Yun, T. A. Hamilton, D. M. Park, A. K. Boal, J. A. Cotruvo, Enhanced rare-earth separation with a metal-sensitive lanmodulin dimer. *Nature* **618**, 87–93 (2023).
18. H. Singer, B. Drobot, C. Zeymer, R. Steudtner, L. J. Daumann, Americium preferred: Lanmodulin, a natural lanthanide-binding protein favors an actinide over lanthanides. *Chem. Sci.* **12**, 15581–15587 (2021).
19. T. Hatanaka, N. Kikkawa, A. Matsugami, Y. Hosokawa, F. Hayashi, N. Ishida, The origins of binding specificity of a lanthanide ion binding peptide. *Sci. Rep.* **10**, 19468 (2020).
20. M. Nitz, M. Sherawat, K. J. Franz, E. Peisach, K. N. Allen, B. Imperiali, Structural origin of the high affinity of a chemically evolved lanthanide-binding peptide. *Angew. Chem. Int. Ed.* **43**, 3682–3685 (2004).
21. A. J. Hurd, R. L. Kelley, R. G. Eggert, M.-H. Lee, Energy-critical elements for sustainable development. *MRS Bull.* **37**, 405–410 (2012).
22. R. Pell, L. Tijsseling, K. Goodenough, F. Wall, Q. Dehaine, A. Grant, D. Deak, X. Yan, P. Whattoff, Towards sustainable extraction of technology materials through integrated approaches. *Nat. Rev. Earth Environ.* **2**, 665–679 (2021).
23. D. A. Doyle, J. M. Cabral, R. A. Pfuetzner, A. Kuo, J. M. Gulbis, S. L. Cohen, B. T. Chait, R. MacKinnon, The structure of the potassium channel: Molecular basis of K$^+$ conduction and selectivity. *Science* **280**, 69–77 (1998).
24. A. C. Dolphin, P. A. Insel, T. F. Blaschke, U. A. Meyer, Introduction to the theme "Ion Channels and Neuropharmacology: From the Past to the Future". *Annu. Rev. Pharmacol. Toxicol.* **60**, 1–6 (2020).
25. S. Goutham, A. Keerthi, A. Ismail, A. Bhardwaj, H. Jalali, Y. You, Y. Li, N. Hassani, H. Peng, M. V. S. Martins, F. Wang, M. Neek-Amal, B. Radha, Beyond steric selectivity of ions using ångström-scale capillaries. *Nat. Nanotechnol.* **18**, 596–601 (2023).
26. A. Esfandiar, B. Radha, F. C. Wang, Q. Yang, S. Hu, S. Garaj, R. R. Nair, A. K. Geim, K. Gopinadhan, Size effect in ion transport through angstrom-scale slits. *Science* **358**, 511–513 (2017).
27. J. Abraham, K. S. Vasu, C. D. Williams, K. Gopinadhan, Y. Su, C. T. Cherian, J. Dix, E. Prestat, S. J. Haigh, I. V. Grigorieva, P. Carbone, A. K. Geim, R. R. Nair, Tunable sieving of ions using graphene oxide membranes. *Nat. Nanotechnol.* **12**, 546–550 (2017).
28. R. H. Tunuguntla, R. Y. Henley, Y.-C. Yao, T. A. Pham, M. Wanunu, A. Noy, Enhanced water permeability and tunable ion selectivity in subnanometer carbon nanotube porins. *Science* **357**, 792–796 (2017).
29. J. Shen, G. Liu, Y. Han, W. Jin, Artificial channels for confined mass transport at the sub-nanometre scale. *Nat. Rev. Mater.* **6**, 294–312 (2021).
30. H. Zhang, X. Li, J. Hou, L. Jiang, H. Wang, Angstrom-scale ion channels towards single-ion selectivity. *Chem. Soc. Rev.* **51**, 2224–2254 (2022).
31. E. Hoenig, S. E. Strong, M. Wang, J. M. Radhakrishnan, N. J. Zaluzec, J. L. Skinner, C. Liu, Controlling the structure of MoS2 membranes via covalent functionalization with molecular spacers. *Nano Lett.* **20**, 7844–7851 (2020).
32. Y. Marcus, A simple empirical model describing the thermodynamics of hydration of ions of widely varying charges, sizes, and shapes. *Biophys. Chem.* **51**, 111–127 (1994).
33. "Ionic conductivity and diffusion at infinite dilution", in *CRC Handbook of Chemistry and Physics, Internet Version 2005*, David R. Lide, ed., CRC Press, 2005.
34. F. Martelli, S. Abadie, J.-P. Simonin, R. Vuilleumier, R. Spezia, Lanthanoids(III) and actinoids(III) in water: Diffusion coefficients and hydration enthalpies from polarizable molecular dynamics simulations. *Pure Appl. Chem.* **85**, 237–246 (2012).
35. C. C. R. Sutton, G. da Silva, G. V. Franks, Modeling the IR spectra of aqueous metal carboxylate complexes: Correlation between bonding geometry and stretching mode wavenumber shifts. *Chem. A Eur. J.* **21**, 6801–6805 (2015).
36. E. R. Nightingale, Phenomenological theory of ion solvation. Effective radii of hydrated ions. *J. Phys. Chem.* **63**, 1381–1387 (1959).
37. P. D'Angelo, R. Spezia, Hydration of lanthanoids(III) and actinoids(III): An experimental/theoretical saga. *Chem. A Eur. J.* **18**, 11162–11178 (2012).
38. A. J. Medford, A. Vojvodic, J. S. Hummelshøj, J. Voss, F. Abild-Pedersen, F. Studt, T. Bligaard, A. Nilsson, J. K. Nørskov, From the Sabatier principle to a predictive theory of transition-metal heterogeneous catalysis. *J. Catal.* **328**, 36–42 (2015).
39. S. Hu, W.-X. Li, Sabatier principle of metal-support interaction for design of ultrastable metal nanocatalysts. *Science* **374**, 1360–1365 (2021).
40. R. Epsztein, R. M. DuChanois, C. L. Ritt, A. Noy, M. Elimelech, Towards single-species selectivity of membranes with subnanometre pores. *Nat. Nanotechnol.* **15**, 426–436 (2020).
41. J. R. Werber, M. Elimelech, Permselectivity limits of biomimetic desalination membranes. *Sci. Adv.* **4**, eaar8266 (2018).
42. X. Zhou, Z. Wang, R. Epsztein, C. Zhan, W. Li, J. D. Fortner, T. A. Pham, J.-H. Kim, M. Elimelech, Intrapore energy barriers govern ion transport and selectivity of desalination membranes. *Sci. Adv.* **6**, eabd9045 (2020).
43. M. Laing, Gadolinium: Central metal of the lanthanoids. *J. Chem. Educ.* **86**, 188 (2009).
44. W. Humphrey, A. Dalke, K. Schulten, VMD: Visual molecular dynamics. *J. Mol. Graph.* **14**, 33–38 (1996).
45. J. Liu, J. Zeng, C. Zhu, J. Miao, Y. Huang, H. Heinz, Interpretable molecular models for molybdenum disulfide and insight into selective peptide recognition. *Chem. Sci.* **11**, 8708–8722 (2020).
46. J. Wang, R. M. Wolf, J. W. Caldwell, P. A. Kollman, D. A. Case, Development and testing of a general amber force field. *J. Comput. Chem.* **25**, 1157–1174 (2004).
47. A. Sengupta, Z. Li, L. F. Song, P. Li, K. M. Merz, Parameterization of monovalent ions for the OPC3, OPC, TIP3P-FB, and TIP4P-FB water models. *J. Chem. Inf. Model.* **61**, 869–880 (2021).
48. Z. Li, L. F. Song, P. Li, K. M. Merz, Parametrization of trivalent and tetravalent metal ions for the OPC3, OPC, TIP3P-FB, and TIP4P-FB water models. *J. Chem. Theory Comput.* **17**, 2342–2354 (2021).
49. P. Eastman, J. Swails, J. D. Chodera, R. T. McGibbon, Y. Zhao, K. A. Beauchamp, L.-P. Wang, A. C. Simmonett, M. P. Harrigan, C. D. Stern, R. P. Wiewiora, B. R. Brooks, V. S. Pande, OpenMM 7: Rapid development of high performance algorithms for molecular dynamics. *PLOS Comput. Biol.* **13**, e1005659 (2017).
50. D. Hill, Diffusion coefficients of nitrate, chloride, sulphate and water in cracked and uncracked Chalk. *J. Soil Sci.* **35**, 27–33 (1984).
51. Z. Li, R. P. Misra, Y. Li, Y.-C. Yao, S. Zhao, Y. Zhang, Y. Chen, D. Blankschtein, A. Noy, Breakdown of the Nernst–Einstein relation in carbon nanotube porins. *Nat. Nanotechnol.* **18**, 177–183 (2023).

52. M. Heiranian, A. B. Farimani, N. R. Aluru, Water desalination with a single-layer MoS2 nanopore. *Nat. Commun.* **6**, 8616 (2015).

53. T. Darden, D. York, L. Pedersen, Particle mesh Ewald: AnN·log(N) method for Ewald sums in large systems. *J. Chem. Phys.* **98**, 10089–10092 (1993).

54. S. Kumar, J. M. Rosenberg, D. Bouzida, R. H. Swendsen, P. A. Kollman, THE weighted histogram analysis method for free-energy calculations on biomolecules. I. The method. *J. Comput. Chem.* **13**, 1011–1021 (1992).

55. Z. Li, L. F. Song, P. Li, K. M. Merz, Systematic parametrization of divalent metal ions for the OPC3, OPC, TIP3P-FB, and TIP4P-FB water models. *J. Chem. Theory Comput.* **16**, 4429–4442 (2020).